Int. J. Electrochem. Sci., 15 **(2020)** 7833 – 7847, doi: 10.20964/2020.08.63

International Journal of
ELECTROCHEMICAL
SCIENCE
www.electrochemsci.org

Oxidation and Corrosion Behavior of (Cu-10Cu_2O) - ($NiFe_2O_4$-10NiO) Cermet Inert Anode with Interpenetrating Structure

Yu-qiang Tao[1,2,3], Zhi-you Li[2], Hai-peng Shao[1], Yu-long Chen[1]

[1] School of Chemistry and Chemical Engineering, University of South China, Hengyang 421001, PR China;
[2] State Key Laboratory of Powder Metallurgy, Central South University, Changsha, 410083, PR China;
[3] Hunan key laboratory for the design and application of actinide complexes, Hengyang, 421001, PR China.
*E-mail: taoyuqiang26@qq.com

Received: 5 April 2020 / *Accepted:* 20 May 2020 / *Published:* 10 July 2020

Cermet anodes with a composition of 26 wt % (Cu - 10 Cu_2O), 74 wt % ($NiFe_2O_4$ - 10 NiO), and interpenetrating structure were prepared via the pressureless infiltration. The air oxidation and electrolytic corrosion in cryolite molten salt of the cermets were studied concerning related microstructure evolution. Results showed that external diffusion oxidation of Cu was the main oxidation mechanism, which led to the formation of a porous zone between the oxidation and un-oxidation zone. The oxidation depth increased along with the higher oxidation temperature; an oxidation depth of 380 μm was confirmed when oxidized at 960 °C for 12 h. The corrosion resistance of the anodes with and without pre-oxidation treatment was similar. The influence of electrolyte on the corrosion was more important than that of the temperature. The corrosion became more serious as the decrease of electrolysis temperature from 960 °C to 800 °C, casued by the decreased current density. With the decrease of current density in the range of 0.2 A/cm^2 - 0.8 A/cm^2, a dense surface layer was more easily formed on the anode bottom. The corrosion of copper oxides was also related to the current density. As the decrease of current density, the corrosion of copper oxide became slower. The side and the bottom were hard to construct synchronously a dense surface layer owing to the uneven electrical distribution.

Keywords: Inert anode; aluminum electrolysis; interpenetrating structure; high temperature oxidation; molten corrosion

1. INTRODUCTION

Currently, the aluminum electrolysis process is carried out in Hall - Héroult cell, in which the anode is carbon material and highly corrosive cryolite is adopted as the electrolyte. Consumable carbon anode reacts with oxygen and electrolyte, generating CO_2, CF_n and other greenhouse gases during the electrolysis process. Hence, it has become an urgent goal to replace the carbon anode with an inert anode

(non-consumable) for the production of aluminum, given environmental perspective [1-2]. Nickel ferrite ($NiFe_2O_4$) based cermets [3-5] and Cu based alloy [6-8] have received a lot of attention as the candidates of inert anode materials, owing to their good corrosion resistance in cryolite electrolyte and low cost. $NiFe_2O_4$-based cermets contained 17 wt % metallic phase have been tested in pilot scale cells for 25 d and 28 d [9-10], respectively. However, the cracking of the cermet anodes and the breakage of the anode conductor stems in pilot cell aluminum electrolysis impeded the application, which became the main objectives in this research field. Moreover, the electrical conductivity of this type anode was less than 90 S/cm, which was much lower than that of carbon anode (~ 200 S/cm).

To improve the mechanical property and conductivity of the cermet anode, a great deal of work has been done [11-13]. Increasing the metallic phase content was an effective way to improve both the mechanical property and the conductivity of the anode [14-15]. However, the increase of metallic phase content is likely to affect the corrosion resistance of the cermet anode, because the corrosion resistance of the metallic phase was worse than that of the ceramic phase [16]. Corrosion resistance is the most important parameter for the inert anode, which plays a crucial role in the aluminum quality and anode life. Recently, (Cu-Ni-Fe) - ($NiFe_2O_4$-NiO) cermet with a metallic phase content of 40 wt % was prepared and used as the anode for 200 A bench scale aluminum electrolysis, which showed excellent corrosion resistance after over 1000 h test[5]. However, Ni is preferentially corroded [17]. Tarcy [18] reported that Cu was passivated in the electrolysis process and considered that cermet anode with continuous copper metallic phase would be conductive and corrosion resistant to cyolite electrolyte. Feng et al. [19] found that the corrosion rate of Cu_2O / Cu cermet was about 1.8 - 1.9 cm / y, and the corroded Cu could react with electrolytic Al and form a useful Cu-Al alloy. However, dense Cu / $NiFe_2O_4$ cermets were hard to be prepared for the bad wettability between $NiFe_2O_4$ and Cu. The study about the corrosion behavior of Cu / $NiFe_2O_4$ cermets with high metallic phase content was little.

Lots of studies about the anode corrosion have been done. Studies showed that the corrosion of $NiFe_2O_4$ based cermet anodes and alloy anodes was affected by many factors, such as anode composition [20], current density [21-22], electrolysis temperature [23], and pre-oxidation treatment [24]. And researchers thought low temperature electrolysis (lower than 950 °C) was a tendency for aluminum electrolysis, which was achieved by adjusting the composition of the electrolyte [25]. At present, most of the electrolysis temperature and current density for $NiFe_2O_4$ based cermets were about 960 °C and 1 A/cm^2, respectively. And pre-oxidation treatment was mainly used for alloy anode other than $NiFe_2O_4$ based cermet [24]. Additionally, research on the corrosion of the anode side was little, which was very important for the anode shape design. In previous studies, the anode corrosion was evaluated mainly by detecting the content of impurities in the cathode aluminum and the electrolyte, which was difficult to study the side corrosion and easily affected by the exfoliation and corrosion production of the furnace material and the conductor stem.

The microstructure of cermet anode with interpenetrating structure is different from that of ceramic based cermet anode and alloy anode, and their corrosion resistance may be different. The electrolysis parameters, especially the current density and the electrolysis temperature, need to be further studied. Additionally, inert anode was partially immersed in the electrolyte in the electrolysis proceed, and the anode was suffered from both atmosphere oxidation and electrolytic corrosion. It needs to

comprehensively consider the atmosphere oxidation and electrolytic corrosion characteristic of the inert anode.

To the best of our knowledge, there is very little literature about the corrosion resistance of (Cu-10Cu_2O) - ($NiFe_2O_4$-10NiO) cermet with interpenetrating structure. Based on our preliminary work [11], the air oxidation and electrolytic corrosion of (Cu-10Cu_2O) - ($NiFe_2O_4$-10NiO) cermet with interpenetrating structure were studied in this paper, and the effects of pre-oxidation, electrolysis temperature and current density on the corrosion resistance of the cermet anode were assessed. A gap was fabricated on the anode bottom and the change in the size of the gap was used to study the anode corrosion.

2. EXPERIMENTAL PROCEDURES

2.1 Preparation of the cermets

(Cu - 10 Cu_2O) - ($NiFe_2O_4$ - 10 NiO) cermets with a composition of 26 wt % (Cu - 10 Cu_2O), 74 wt % ($NiFe_2O_4$ - 10 NiO), and interpenetrating structure were prepared via the pressureless infiltration, as described in the previous report [11]. $NiFe_2O_4$ - 10 NiO ceramic was synthesized by solid-state reaction. Commercial Fe_2O_3 (99.60 %, 0.75 μm, JFE Chemical Co., Japan) and NiO (77.64 wt% Ni, Jinchuan Group Ltd., China) powders were mixed in a mass ratio of 1 to 1.6 and ball-milled in ethanol and zirconia media for 10 h. The mixture was dried at 100 °C and then calcined at 1200 °C for 6 h in air. The mixture composed of 10 wt% Cu_2O (Tianjin Guangfu Fine Chemical Research Institute, China) and 90 wt% Cu (99.5 %, 9.86 μm, Gripm Advance Materials Co., China) powders was employed as infiltrant. The synthesized ceramic powder and the infiltrant were respectively pressed into 105 mm × 45 mm × 25 mm and 105 mm × 45 mm × 9 mm plates by die-pressing at 80 MPa, followed by cold isostatic pressing at 150 MPa. The ceramic compact was pre-sintered at 1200 °C for 6 h. The infiltrant was put on $NiFe_2O_4$ - 10 NiO preform in a vacuum furnace, and heated to 1200 °C at 5 °C / min and held for 2 h in 0.04 MPa static N_2 atmosphere with an oxygen partial pressure of ~10 Pa, and then the furnace was cooled spontaneously to room temperature. According to calculation, the infiltrated metallic phase content in the resulting composite was about 26 wt %.

2.2 Oxidation and electrolysis tests

The as-sintered cermets were sliced to blocks (about 23 mm × 20 mm × 20 mm) and sheets (about 15 mm × 15 mm × 2 mm) for electrolysis tests and oxidation tests, respectively. The surfaces of the blocks and the sheets were polished using diamond polishing suspensions, and cleaned by ethanol using an ultrasonic bath. The oxidation tests were carried out in a muffle furnace in air at temperatures between 800 °C and 960 °C. Sheets were put in an Al_2O_3 crucible and heated at 8 °C / min to the oxidation temperature and held for 12 h, and then the crucible was withdrawn and cooled spontaneously to room temperature.

A gap (named as pre-fabricated gap) in the anode (block sample) bottom was made using a diamond cutting machine. The anode used to study the effect of pre-oxidation on corrosion resistance was oxidized in air at 880 °C for 24 h before electrolysis test, and the oxide scale on one side of the pre-fabricated gap was removed by sandpaper before electrolysis. Other anodes were oxidized at 880 °C for 12 h before electrolysis.

The process of electrolysis test was similar to the previous report [26]. The anode samples were glued to a guide rod (316 stainless-steel) by a high-temperature conductive adhesive. The assembled anode was heated together with the cryolite electrolyte, and the anode was 10 mm above the electrolyte. After the electrolyte was heated to the electrolysis temperature for 0.5 h, the anode was immersed in the electrolyte 10 mm. The electrolysis temperatures were 800 °C, 880 °C, and 960 °C, respectively, and the corresponding electrolyte composition and parameter were shown in Table 1. The current densities were 0.2 A/cm^2, 0.5 A/cm^2, 0.8 A/cm^2, and 1.0 A/cm^2, respectively, based on the bottom area of the anode. After electrolysis, the anodes were sectioned along the axial direction of the guide rod and polished for microstructure characterization.

Table 1. Composition and parameter of the electrolyte used in electrolysis test

Electrolysis temperature /℃	Electrolyte composition / wt%						Melting point / ℃	Solubility of Al_2O_3 / wt%
	Na_3AlF_6	AlF_3	CaF_2	Al_2O_3	K_3AlF_6	LiF		
960	78.07	9.5	5.0	7.43	/	/	947	7.13
880	51.39	24.0	/	4.48	17.13	3	875	4.23
800	42.18	24.7	/	5	28.12	/	772	2.71

2.3 Characterization

The phase compositions were examined by X-ray diffraction (XRD) (Rigaku D/max 2550VB+, Rigaku Corporation, Tokyo, Japan) with Cu K_α radiation (λ = 0.154 nm). The microstructural analysis was performed by scanning electron microscopy (SEM) (FEI Quanta 200, FEI Company, Eindhoven, the Netherlands), and the element contents in different phases were analyzed by energy dispersive spectroscopy (EDS) (EDX-GENESIS 60S, EDAX Company of America, Mahwah, NJ, USA). The oxidation and corrosion depths were measured through the SEM images of the cermets.

3. RESULTS AND DISCUSSION

3.1 Microstructures of the as-sintered cermets

Fig. 1 shows the micrographs, XRD and EDS results of the as-sintered cermet. The cermet was mainly composed of $NiFe_2O_4$, NiO, Cu_2O, and Cu phases, as shown in Fig. 1 (b). $NiFe_2O_4$ phase had a net-like framework structure, whose sintering necks were formed, and the surface of most $NiFe_2O_4$ grains next to Cu or Cu_2O grains was cambered, as shown in Fig. 1 (a). NiO grains were isolated and no obvious $NiFe_2O_4$ precipitate was found in NiO grains. Cu phase exhibited an approximate network

structure. According to the EDS, as shown in Fig. 1 (c), the Fe / Ni atomic ratio of $NiFe_2O_4$ phase was about 2.2, and the Fe / Ni atomic ratio of NiO phase was 0.12, and Cu phase contained a little of Fe (about 6 at%) and Ni (about 2 at%), which were similar to the previous infiltrated samples [11].

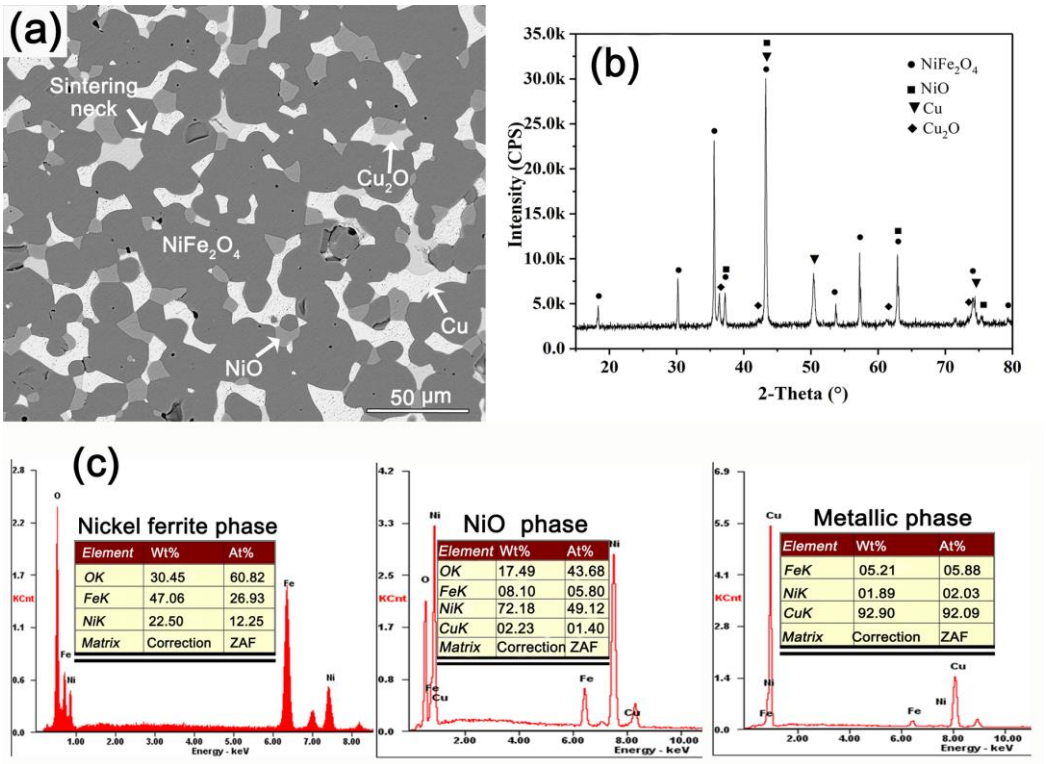

Figure 1. Micrographs (a), XRD (b) and EDS (c) of the as-sintered cermet

3.2 Microstructures of the cermets oxidized in air

Fig. 2 shows the XRD of the cermet surface after oxidation at 850 °C for 12 h. The surface layer mainly comprised CuO, Cu_2O, and $NiFe_2O_4$ phases.

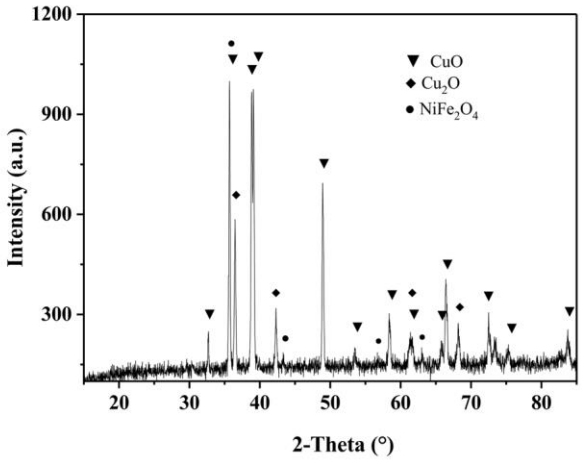

Figure 2. XRD of the cermet surface oxidized in air at 850 °C for 12 h

Table 2. Internal oxidation depth of the cermets oxidized at different temperatures

Oxidation temperature, °C	Internal oxidation depth, μm	Oxidation temperature, °C	Internal oxidation depth, μm
800	86	880	167
850	154	960	386

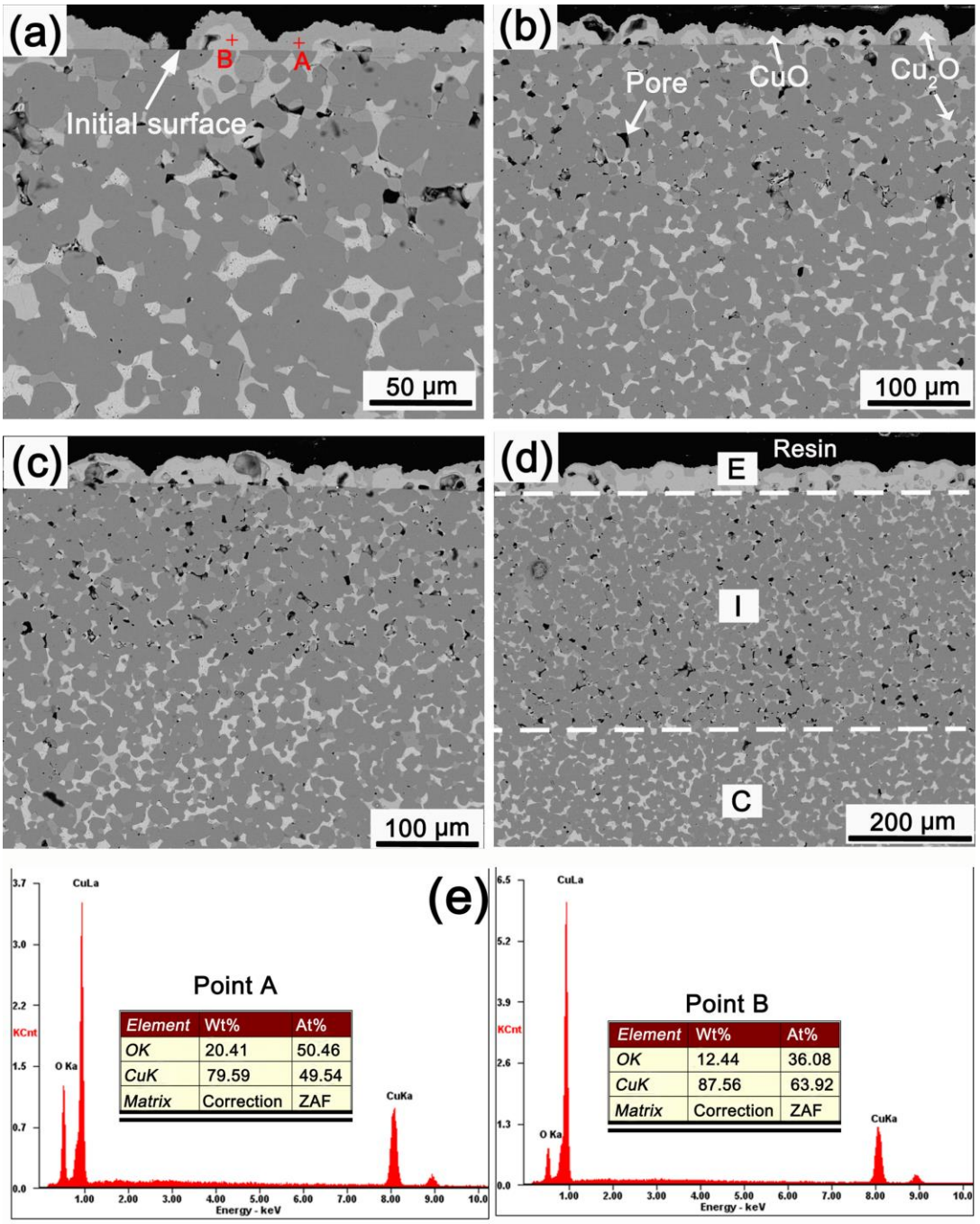

Figure 3. Cross sectional micrographs and EDS of the cermets oxidized in air at different temperatures for 12 h: (a) 800 °C; (b) 850 °C; (c) 880 °C; (d) 960 °C; (e) EDS of points A and B in (a)

Fig. 3 shows the cross sectional microstructures of the cermets after oxidation in air at 800 - 960 °C for 12 h. All the oxidized cermets were composed of three different characterization zones [labeled E, I and C in Fig. 3 (d)]. Zone E was composed of two phases. According to the EDS results in Fig. 3 (e), the Cu / O atomic ratios of the dark gray phase (Point A) and the light gray phase (Point B) in Fig.3 (a) were 0.98 and 1.77, respectively. Points A and B should be CuO phase and Cu_2O phase, respectively. No $NiFe_2O_4$ was found in zone E, indicating that zone E was formed by external oxidation. Zone I mainly comprised of $NiFe_2O_4$, Cu_2O, and NiO phases and was more porous than zone C. The pores were mainly distributed at the interface between zone I and zone C. The morphology of the pore next to zone C was similar to that of the metallic particles. The pores should result from the outward diffusion of the metallic phase, similar to the case of Cu rich Cu-Ni alloy [27]. The surface of $NiFe_2O_4$ grain next to the pores was cambered and the grains did not coarsen when oxidized at 960 °C, indicating that no obvious sintering of the ceramic phase occurred in the oxidation process. Table 2 shows the internal oxidation depths of the cermets oxidized at different temperatures. The higher the oxidation temperature, the deeper zone I was. And the part of Zone I next to Zone E became dense as the increase of oxidation temperature. The morphology of zone C was similar to that of the as-sintered cermet, and zone C should be the non-oxidized zone.

The oxidation process was similar to that of 40 wt% (20Ni-80Cu) / 60 wt% ($NiFe_2O_4$-10NiO) cermet [28]. The morphology of the porous oxide scales was related to the morphology and composition of the metallic phase and the out-diffusion characteristic of Cu. The Cu exposing to air could react with oxygen in air to form CuO above 800 °C based on the thermodynamic calculation [29]. Oxygen concentration gradient was formed within the cermet due to the formation of CuO on the initial surface, and the stable phase Cu_2O was the main oxidation product of zone I at low-oxygen partial pressure. Cu_2O is metal-deficient, and the predominant point defects are metal vacancies [30]. The outward diffusion of Cu is faster than the inward diffusion of oxygen, as the Cu atomic radius (0.157 nm) is much smaller than that of oxygen (0.78 nm), leading to the formation of a porous zone in oxidation front. Cu could outward diffuse without getting through the ceramic phase when the network structure of the Cu phase was formed, which was beneficial for the external oxidation of Cu and the formation of a porous oxide scale.

According to the Arrhenius equation, as shown in formula (1), increasing the oxidation temperature could accelerate the diffusion rate of Cu and oxygen. The higher the oxidation temperature, the higher the internal oxidation depth was. The Cu far from the surface, especially at high oxidation temperature, would be oxidized by the internal diffusion oxygen before diffusing to the surface. Partial pores next to zone E generated by the external diffusion of Cu were filled by oxidation product, since volume expansion induced by the oxidation of higher density metallic phase Cu (8.9 g/cm^3) to lower density oxides Cu_2O (6.0 g/cm^3). Therefore, zone I that next to zone E was dense.

$$K_p = A \exp\left(\frac{-E_a}{RT}\right) \quad (1)$$

Where K_p is the oxidation rate constant, R is the molar gas constant, T is the oxidation temperature, E_a is the oxidation activation energy, and A is the exponential factor. It can be assumed that A and E_a do not vary with temperature within a certain temperature.

3.3 Electrolytic corrosion

3.3.1 Pre-oxidation treatment

Fig. 4 shows the micrographs of the pre-oxidized anode bottom after electrolysis at 960 °C for 24 h. It was composed of three different characterization zones [labeled P, O, and U]. Zone P was mainly composed of $NiFe_2O_4$ phase. A small amount of CuO, NiO, and aluminate were also found in this zone. Compared with Fig. 3 (d), the external oxidation layer (zone E) formed in the pre-oxidation process was dissolved. The $NiFe_2O_4$ grains exposing to electrolyte were significantly corroded and fragmented. The part that next to electrolyte was denser than the other part of zone P. A few large $NiFe_2O_4$ grains were found in the denser part. The morphology of zone O was similar to that of the inner oxidation zone of the sample oxidized in air, mainly containing Cu_2O and $NiFe_2O_4$ phases and a lot of small pores. Electrolyte was found in the pores of zone O. The corrosion depths (both zones P and O) for the parts with and without pre-oxidation scales were 1160 μm and 1150 μm, respectively. And the corrosion depth of reported Fe-32Ni alloy was about 1900 μm when electrolyzed at 940 °C for 30 min at a current density of 1.5 A/cm^2 [31].

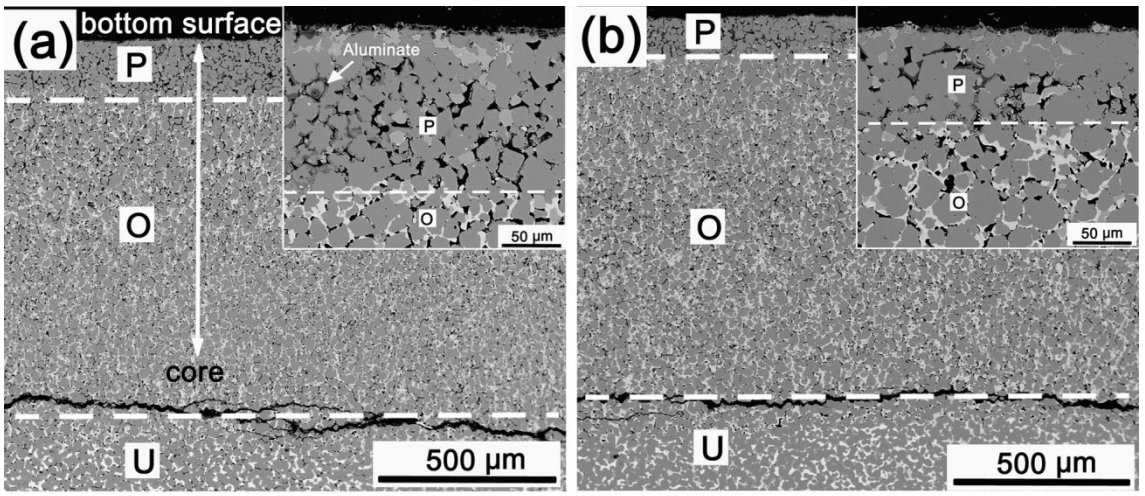

Figure 4. Micrographs of the pre-oxidized cermet bottoms after electrolysis at 960 °C for 24 h: (a) without pre-oxidation scale; (b) with pre-oxidation scale; insets were the magnifications of corrosion zones

The effect of pre-oxidation treatment on the anode corrosion resistance was not as well as that of Ni-Fe alloy anode formed a corrosion resistant spinel-rich layer in the anode surface, which could avoid electrochemical corrosion of the metallic phase [24]. The main reasons are the poor oxidation resistance of the anode, and the higher solubility of copper oxides compared to that of NiO and $NiFe_2O_4$ [32, 33] and the difficulty in forming copper aluminum oxide. The metallic phase in the surface without pre-oxidation scale was rapidly oxidized and a CuO dense external oxide scale formed for the poor oxidation resistance of Cu in the pre-heating process. Then the morphologies of the two parts with and without

pre-oxidation scale would be similar before immersing into the electrolyte, resulting in a similar corrosion depth.

3.3.2 Electrolysis temperature

Fig. 5 shows the micrographs of the anode bottoms after electrolysis at different temperatures. The corrosion depths were about 2310 μm, 1300 μm and 850 μm when electrolyzed at 800 °C, 880 °C and 960 °C, respectively. The corrosion zone electrolyzed at 960 °C was much denser than that electrolyzed at 800 °C and 880 °C. For 800 °C electrolysis, a swelling layer was formed on the anode surface and the swelling layer close to electrolyte was mainly composed of AlF_3, $NiFe_2O_4$, Fe_2O_3, and NiF_2, as shown in Fig. 6. And the inner corrosion zone was mainly composed of $NiFe_2O_4$ (point 1), NiF_2 (point 2), and Cu_2O (point 3) phases based on the EDS results as shown in Table 3. For 880 °C electrolysis, the outermost layer was mainly composed of aluminate (point 4) and $NiFe_2O_4$ (point 5). Selected zone 2 in Fig. 5 (b) was mainly composed of $NiFe_2O_4$ and electrolyte. No obvious aluminate was found in selected zone 2. For 960 °C electrolysis, the surface layer close to the electrolyte was denser than the internal corrosion zone, which was different from that electrolyzed at 800 °C and 880 °C. CuO, Cu_2O, and a trace of aluminate were also found in the surface layer besides $NiFe_2O_4$. And electrolyte was also found inside the pores.

It could be inferred from above that the corrosion of the anode was closely related to the electrolysis temperature or the electrolyte composition. With the increase of AlF_3 and K_3AlF_6 in electrolyte, the electrolysis temperature and the solubility of Al_2O_3 decrease, as shown in Table 1. And $NiFe_2O_4$ could react with AlF_3 to form NiF_2 and Fe_2O_3, as shown in equation (1) [34]. Increasing the content of AlF_3 was favorable for the reaction of equation (1) to the right, and the catastrophic corrosion of $NiFe_2O_4$ occurred when the AlF_3 concentration was high, resulting in the formation of NiF_2 and the porous surface. Al_2O_3 exists in the electrolyte mainly in the form of $Al_2O_2F_4^{2-}$ [35], which could react with the ceramic phase to form aluminates at high temperature, as shown in reactions (2) and (3). The formation of aluminate was difficult under a low Al_2O_3 concentration [36]. The $FeAl_2O_4$ and $NiAl_2O_4$ could exist at 1020 °C only when the concentrations of Al_2O_3 in electrolysis were above 5 wt % and 3 wt %, respectively [37]. Additionally, the higher the temperature, the more easily occurred the reactions (2) and (3) were. Therefore, the aluminates with good corrosion resistance were more easily formed at high temperature electrolysis. The solubility of the oxide also related to the temperature and CR (molar ratio of NaF / AlF_3) [32-33]. And the solubility of copper oxides decreased as the increase of CR [32]. So the copper oxides were not found on the anode surface and the surface layer was porous when electrolyzed at 800 °C and 880 °C. When the influence of electrolyte on the corrosion was more important than that of the temperature, the corrosion of anode electrolyzed at low temperature would be more serious than that electrolyzed at high temperature.

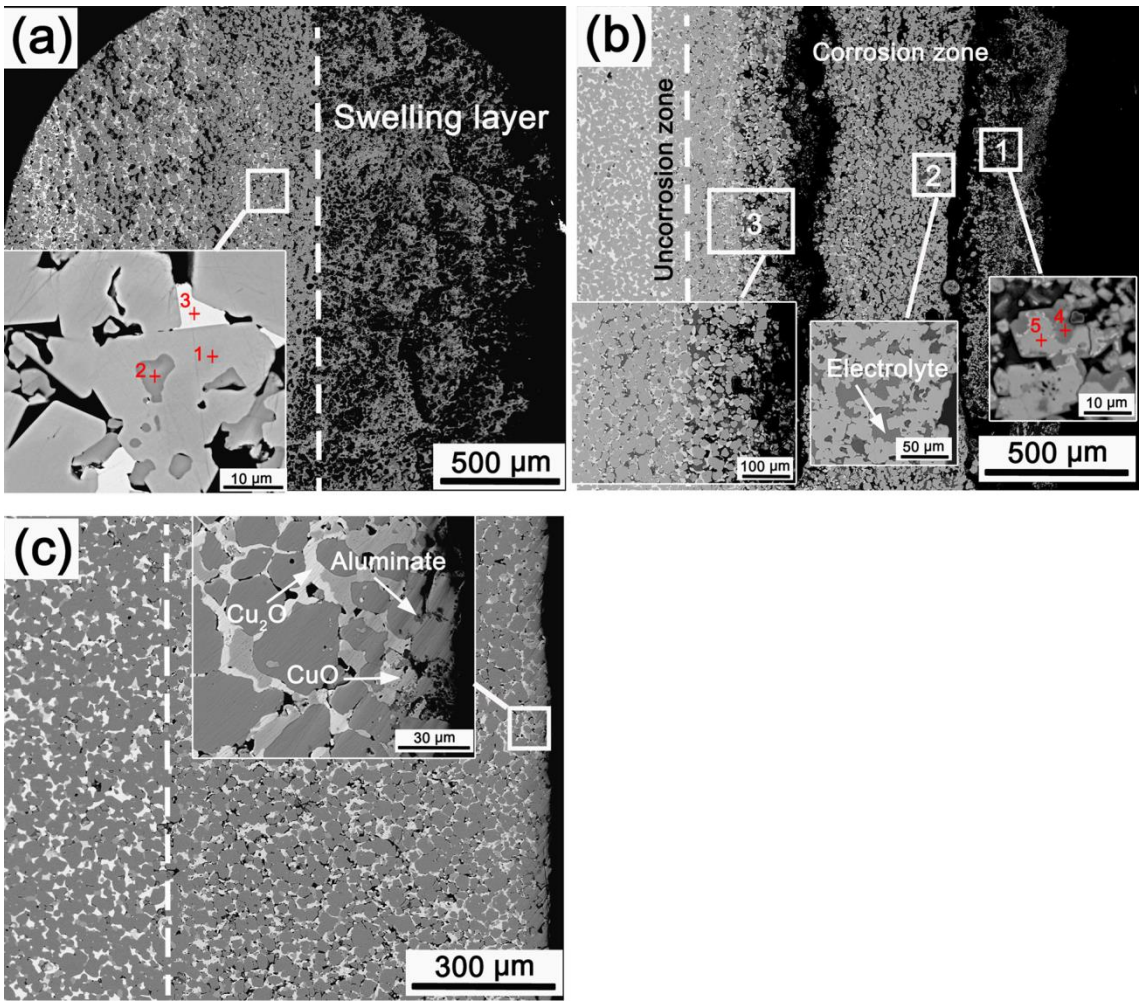

Figure 5. Micrographs of the anode bottoms after electrolysis at different temperatures: (a) 800 °C; (b) 880 °C; (c) 960 °C

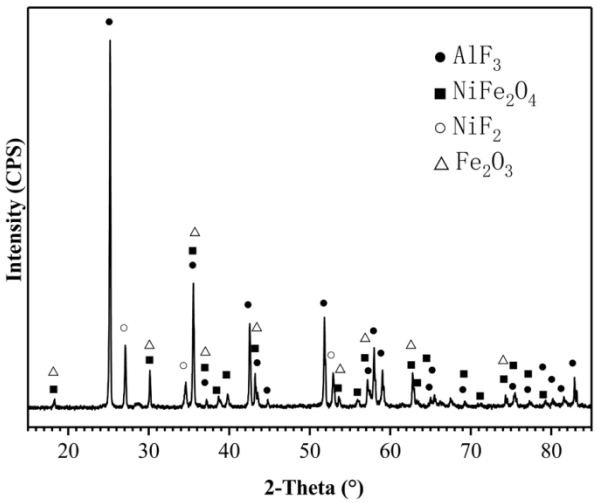

Figure 6. XRD pattern of the swelling layer of the anode electrolyzed at 800 °C

Table 3. Element contents of different phases at different locations in Figure 5

Element	Point 1 phase	Point 2 phase	Point 3 phase	Point 4 phase	Point 5 phase
O / at%	61.13	/	53.06	27.66	31.13
F / at%	/	69.33	/		/
Fe / at%	24.85	2.56	3.01	12.92	43.26
Ni / at%	10.62	28.11	/	17.00	21.55
Cu / at%	3.40	/	43.93	4.35	4.06
Al / at%	/	/	/	38.07	/

$$6\ NiO{\cdot}Fe_2O_3 + 4\ AlF_3 = 6\ NiF_2 + 6\ Fe_2O_3 + 4\ Al + 3\ O_2 \quad (1)$$

$$3\ Al_2O_2F_4^{2-} + NiO = NiAl_2O_4 + O + 2\ Al_2OF_6^{2-} + 2e \quad (2)$$

$$3\ Al_2O_2F_4^{2-} + FeO = FeAl_2O_4 + O + 2\ Al_2OF_6^{2-} + 2e \quad (3)$$

3.3.3 Current density

Fig. 7 shows the micrographs of the anode bottoms and the pre-fabricated gaps that electrolyzed at different current densities. As the current density decreased, the outermost layer of the bottom became denser. When the current density was reduced to 0.5 A/cm^2, a dense layer (labeled D) was formed in the surface of the bottom, as shown in Fig. 7 (c). And a porous layer (labeled L) existed on the inner side of layer D. It could found that the aluminate was mainly distributed at the pore edge of layer L from the insets of Fig. 7 (a). There was also a small amount of aluminate in the anode surface next to the electrolyte, and almost no aluminate was found in layer D. With the decrease of current density, the surface of the pre-fabricated gap became loose and porous. The pre-fabricated gap was filled with Cu_2O phase when the current density was 0.2 A/cm^2, indicating that the dissolution of Cu_2O was slow at low current density. And there was no Cu_2O phase in the gaps when the current density was 0.5 A/cm^2 or 0.8 A/cm^2. Instead, electrolyte and $NiFe_2O_4$ grains were found in the gap when electrolyzed at a current density of 0.5 A/cm^2.

Table 4. Corrosion depths of the anode and the widths of the pre-fabricated gaps electrolyzed at 960 °C with different current densities

Current density , A/cm^2	Zone D, μm	Zone L, μm	Zone I, μm	Total corrosion depth, μm	Gap width before electrolysis, μm	Gap width after electrolysis, μm
0.8	unobvious	95	1065	1160	388	331
0.5	160	200	1013	1373	420	370
0.2	193	183	1044	1420	351	311

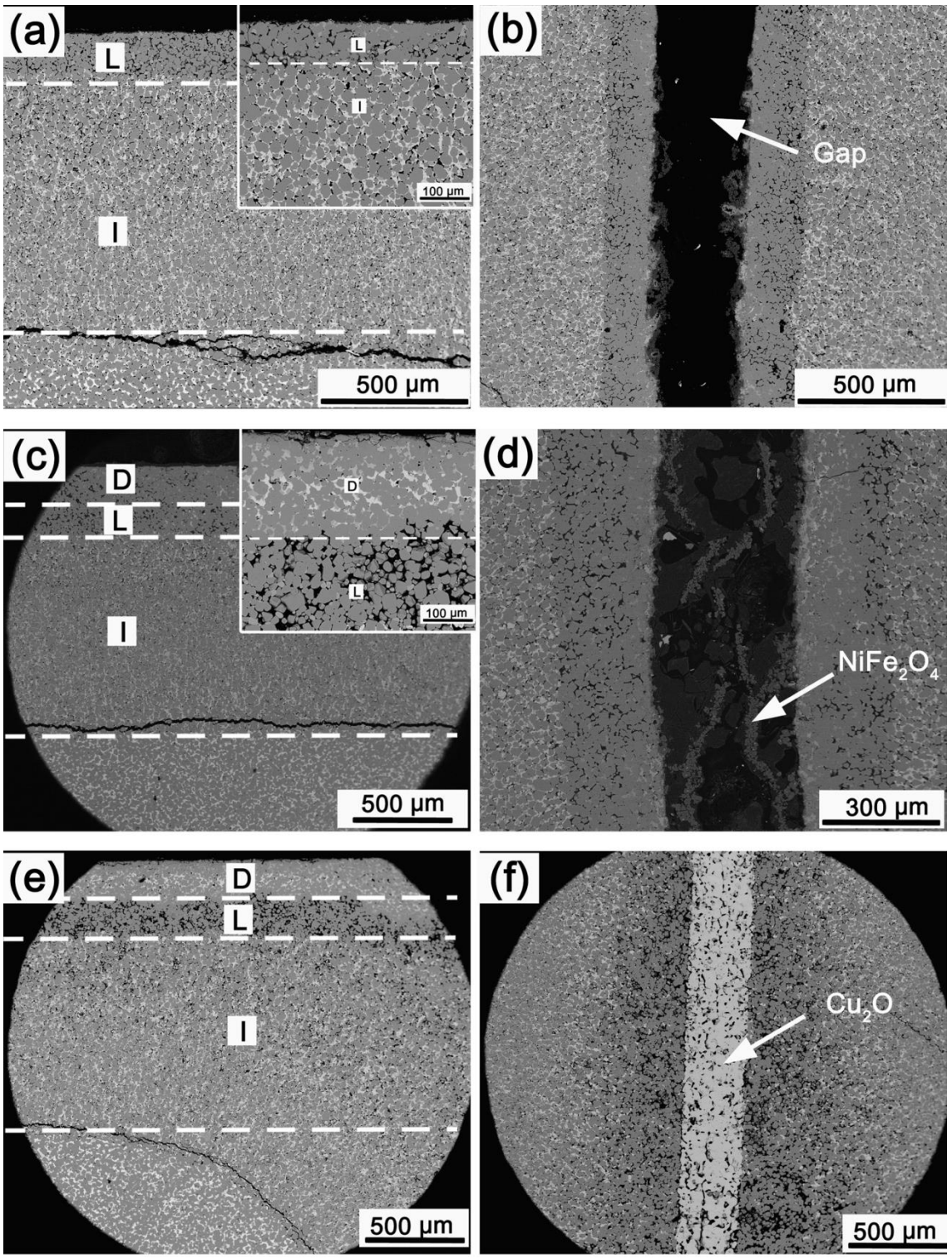

Figure 7. Micrographs of the anode bottoms and the pre-fabricated gaps after electrolysis at different current densities at 960 °C: (a) and (b) 0.8 A/cm^2; (c) and (d) 0.5 A/cm^2; (e) and (f) 0.2 A/cm^2; (a), (c), (e) were the bottoms and (b), (d), (f) were the gaps

Table 4 shows the corrosion depths of the anodes and the widths of the pre-fabricated gaps before and after electrolysis at different current densities at 960 °C. The total corrosion depth of the anode bottom decreased and the widths of the pre-fabricated gap narrowed down as the current density

decreased. The widths of the pre-fabricated gap were reduced by about 14.7 %, 11.9 % and 11.4 % when current density was 0.8 A/cm^2, 0.5 A/cm^2 and 0.2 A/cm^2, respectively.

The content and productivity of atomic oxygen produced by the anodic reaction and the electrochemical corrosion of the anode were related to the current density according to Faraday's laws, as shown in equations (4) and (5). The current passing through the side of the anode was about 15 % of the total current [38], so the current density of the side was very small especially when electrolyzed at low current density, e.g. 0.2 A/cm^2. Then the side of anode should be mainly corroded by the chemical dissolution and oxidation at low current density. The copper oxides formed through external oxidation would fill the gap when the dissolution of copper oxidation was slow, as shown in Fig. 7 (f). And the anode bottom should occur electrochemical corrosion, dissolution corrosion, and oxidation. As the increase of current density, the electrochemical corrosions of both the bottom and the side became serious, and the electrochemical corrosion became the main corrosion form. The copper oxides were preferentially dissolved because its corrosion resistance was weaker than that of $NiFe_2O_4$ and NiO, then a porous bottom was formed, as shown in Fig. 7 (a).

$$O^{2-} + 4e = O_2 \quad (4)$$

$$m = \left(\frac{It}{F}\right) \times \left(\frac{M}{z}\right) \quad (5)$$

Where m is the mass of the substance liberated at an electrode in g; I is the current density; t is the total time the constant current was applied; F = 96500 C / mol is the Faraday constant; M is the molar mass of the substance in g / mol; z is the valence number of ions of the substance.

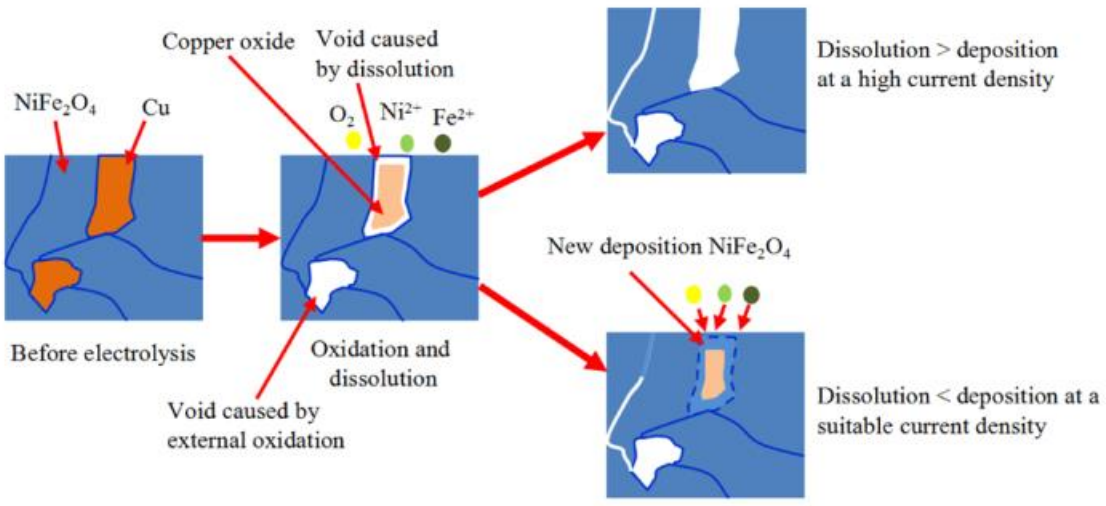

Figure 8. Schematic diagram of the electrolytic corrosion of the cermet anode

Besides of the transition of Ni(Fe)O to $NiFe_2O_4$, the oxidation of Ni and the formation of aluminates [26, 39], the densification of anode surface shown in Fig. 7 (b) - (e) should be also caused by the deposition of small $NiFe_2O_4$ grains exfoliated from the anode, and the precipitation and growth of dissolving $NiFe_2O_4$ grains, as shown in Fig. 8, which was similar to $Ba_{0.5}Sr_{0.5}Co_{0.8}Fe_{0.2}O_{3-\delta}$ anode that allowed a dynamic self-reconstruction of the material's surface during oxygen evolution reaction [40].

This dissolved-redeposition phenomenon was also found in the static molten salt corrosion process of MgO-NiO-Fe_2O_3 ceramics [41]. When the corrosion of copper oxide was slow, the void formed by the dissolution of copper oxide would be replaced by the deposition and grown of $NiFe_2O_4$, which resulted in the densification of the anode surface and the coarsening of $NiFe_2O_4$ grains next to the electrolyte. When the corrosion of ceramic phases was very serious at high current density, the deposition and grown of $NiFe_2O_4$ could not fill the pores, a porous surface would form, as shown in Fig.7 (a).

4. CONCLUSION

For the (Cu - 10Cu_2O) - ($NiFe_2O_4$ - 10NiO) cermet anode with interpenetrating structure, external diffusion oxidation of Cu was the main oxidation mechanism, which resulted in the formation of a porous zone between the oxidation zone and un-oxidation zone. The oxidation depth increased as the oxidation temperature increased from 800 °C to 960 °C. The oxidation depth was up to 380 μm when oxidized at 960 °C for 12 h. The corrosion resistance of the anodes with and without pre-oxidation treatment was similar. The influence of electrolyte on corrosion was more important than the temperature. The corrosion became more serious as the decrease of electrolysis temperature from 960 °C to 800 °C. The current density had a great influence on the electrolytic corrosion of the anode. With the decrease of current density in a range of 0.2 A/cm^2 - 0.8 A/cm^2, the anode bottom was more easily formed a dense surface layer. The corrosion of copper oxides was also related to the current density. As the decrease of current density, the corrosion of copper oxide became slower. The side and the bottom were hard to synchronously form a dense surface layer for the uneven electrical distribution.

ACKNOWLEDGEMENT
This work was supported by the Hunan Provincial Natural Science Foundation of China [2018JJ3447]; the Outstanding Youth Project of Hunan Provincial Department of Education [16B221]; the National High-Tech Research and Development Program of China [2008AA030501]; the Applied Basic Research Program of Hengyang Science and Technology Bureau [2016K153]; the High Level Introduction of Talent Research Start-up Fund of University of South China [2015XQD09]; and the Innovative Experiment Program for College Students [2018XJXZ342], [201910555097].

References

1. R. P. Pawlek, Light Metals 2008, TMS, Warrendale, USA, 2008, 1039.
2. R. P. Pawlek, Light Metals 2014, TMS, Warrendale, USA, 2014, 1309.
3. K. C. Zhou, and Y. Q. Tao, *Chin. J. Nonferrous. Met*., 21 (2011) 2418.
4. Z. Tian, W. Guo, Y. Lai, K. Zhang, and J. Li, *T. Nonferr. Metal. Soc*., 26 (2016) 2925.
5. W. Yang, J. Guo, J. Li, G. Zhang, L. He, and K. Zhou, *J. Am. Ceram. Soc*., 100 (2017) 887.
6. E. Gavrilova, G. Goupil, B. Davis, D. Guay, and L. Roué, *Corros. Sci*., 101 (2015) 105.
7. G. Goupil, S. Jucken, D. Poirier, J. G. Legoux, E. Irissou, B. Davis, D. Guay, and L. Roué, *Corros. Sci.,* 90(2015) 259 .
8. G. Goupil, G. Bonnefont, H. Idrissi, D. Guay, and L. Roué, *J. Alloy. Compd*., 580(2013) 256 .
9. T. R. Alcorn, A. T. Tabereaux, N. E. Richards, C. F. Windisch Jr, D. M. Strachan, J. S. Gregg, and M. S. Frederick, Light Metals 1993, TMS, Warrendale, USA, 1993, 433.

10. Z. L. Tian, Y. Q. Lai, Z. Y. Li, J. Li, K. C. Zhou, and Y. X. Liu, *JOM*, 61 (2009)34.
11. Y. Tao, Z. Li, L. Zhang, X. Gan, and K. Zhou, *J. Am. Ceram. Soc*., 95 (2012) 3739.
12. X. Long, Y. Liu, G. Yao, J. Du, X. Zhang, J. Cheng, and Z. Hua, *J. Alloy. Compd*., 551(2013)444.
13. B. Wang, F. Liang, Y. Wang, and K. Peng, Light Metals 2016, TMS, Warrendale, USA, 2016, 429.
14. R. Rapp, A. Ezis, and G. Yurek, *Metall. Mater. Trans*. B, 4 (1973)1283.
15. D. S. McLachlan, M. Blaszkiewicz, and R. E. Newnham, *J. Am. Ceram. Soc*., 73 (1990)2187 .
16. S. P. Ray and R. A. Rapp, No 4455211, US Patent, 1984.
17. D. A. Simakov, E. V. Antipov, M. I. Borzenko, S. Y. Vassiliev, Y. A. Velikodny, V. M. Denisov, V. V. Ivanov, S. M. Kazakov, Z. V. Kuzminova, A. Y. Filatov, G. A. Tsirlina, and V. I. Shtanov, Light Metals 2007, TMS, Warrendale, USA, 2007, 489.
18. G. P. Tarcy, Light Metals 1986, TMS, Warrendale, USA, 1986, 309.
19. L. C. Feng, N. Xie, W. Z. Shao, L. Zhen, and V. V. Ivanov, *J. Alloy. Compd*., 610 (2014)214.
20. S. Helle, B. Davis, D. Guay, and L. Roue, *J. Electrochem. Soc*., 160 (2013)E55.
21. Z. L. Tian, T. Zhang, C. J. Wei, Y. Q Lai, J. Li, *Chin. J. Nonferrous Met*., 24 (2014)2360.
22. J. H. Yang, J. N. Hryn, and G. K. Krumdick, Light Metals 2006, TMS, Warrendale, USA, 2006, 421.
23. H. Wang, A. F. Zhai, X. Wang, Y. H. Lin, Materials Research and Application, 9 (2015)85.
24. V. Chapman, B. J. Welch, and M. Skyllas-Kazacos, *Electrochim. Acta*, 56 (2011)1227.
25. P. Cui, A. Solheim, G. M. Haarberg, Light Metals 2016, TMS, Warrendale, PA , 2016, 383.
26. J. Y. Liu, Z. Y. Li, Y. Q. Tao, D. Zhang, and K. C. Zhou, *T. Nonferr. Metal. Soc*., 21 (2011)566.
27. R. Haugsrud, *Corros. Sci*., 42(2000)383.
28. Y. Q. Tao, Z. Y. Li, D. Zhang, H. W. Xiong, and K. C. Zhou, *J. Am. Ceram. Soc*., 95 (2012)3031.
29. Y. J. Liang, Y .C. Che, Hand book for thermodynamics data of inorganic matter, Northeastern Univ. Pr., (1993)Shenyang, China.
30. N. Birks, G. H. Meier, and F. S. Pettit, Introduction to the High-temperature Oxidation of Metals, Cambridge Univ Pr, (2006)New York, USA.
31. Y. Huang, Y. Yang, L. Zhu, F. Liu, Z. Wang, B. Gao, Z. Shi, and X. Hu, *Int. J. Electrochem. Sc*., 14 (2019)6325.
32. O. A. Lorentsen, T. E. Jentoftsen, E. W. Dewing, and J. Thonstad, *Metall. Mater. Trans*. B, 38 (2007) 833.
33. D. H. DeYoung, Light Metals 1986, TMS, Warrendale, USA, 1986, 299.
34. B. J. Welch, Light Metals 2009, TMS, Warrendale, USA, 2009, 971.
35. X. Hu, J. Qu, B. Gao, Z. Shi, F. Liu, and Z. Wang, *T. Nonferr. Metal. Soc.,* 21(2011)402.
36. M. Oudot, L. Cassayre, P. Chamelot, M. Gibilaro, L. Massot, M. Pijolat, and S. Bouvet, *Corros. Sci.*, 79(2014)159.
37. T. Jentoftsen, O. A. Lorentsen, E. Dewing, G. Haarberg, and J. Thonstad, *Metall. Mater. Trans*. B, 33(2002)901.
38. J. Zoric, I. R. Ar, and J. Thonstad, *J. Appl. Electrochem*., 27(1997) 916.
39. B. G. Liu, L. Zhang, K. C. Zhou, Z. Y. Li, and H. Wang, *Solid State Sci*., 13 (2011)1483.
40. E. Fabbri, M. Nachtegaal, T. Binninger, X. Cheng, B. Kim, J. Durst, F. Bozza, T. Graule, R. Sch äublin, L. Wiles, M. Pertoso, N. Danilovic, K. E. Ayers, and T. J. Schmidt, *Nat. Mater*., 16(2017)925.
41. Y. Xu, Y. Li, J. Yang, S. Sang, and Q. Wang, *J. Alloy. Compd*., 723 (2017)64.